AGU PUBLICATIONS

JGR

Journal of Geophysical Research: Oceans

RESEARCH ARTICLE

10.1002/2016JC011978

Long-range sediment transport in the world's oceans by stably stratified turbidity currents

Benjamin Kneller[1], Mohamad M. Nasr-Azadani[2], Senthil Radhakrishnan[2], and Eckart Meiburg[2]

[1]School of Geosciences, University of Aberdeen, Kings College, Aberdeen, UK, [2]Department of Mechanical Engineering, University of California at Santa Barbara, Santa Barbara, California, USA

Key Points:
- This work presents a new framework for the long-range propagation of turbidity currents on the low gradients of submarine fan channels
- We emphasize the significance of stable stratification in drag reduction and very low rates of entrainment of ambient water
- Numerical validation in 2-D (DNS) and 3-D (LES) is combined with a selection of published data on flow conditions on submarine fans

Correspondence to:
B. Kneller,
b.kneller@abdn.ac.uk

Citation:
Kneller, B., M. M. Nasr-Azadani, S. Radhakrishnan, and E. Meiburg (2016), Long-range sediment transport in the world's oceans by stably stratified turbidity currents, *J. Geophys. Res. Oceans*, *121*, 8608–8620, doi:10.1002/2016JC011978.

Received 18 MAY 2016
Accepted 9 SEP 2016
Accepted article online 27 OCT 2016
Published online 9 DEC 2016

Abstract Submarine fans, supplied primarily by turbidity currents, constitute the largest sediment accumulations on Earth. Generally accepted models of turbidity current behavior imply they should dissipate rapidly on the very small gradients of submarine fans, thus their persistence over long distances is enigmatic. We present numerical evidence, constrained by published field data, suggesting that turbidity currents traveling on low slopes and carrying fine particles have a stably stratified shear layer along their upper interface, which dramatically reduces dissipation and entrainment of ambient fluid, allowing the current to propagate over long distances. We propose gradient Richardson number as a useful criterion to discriminate between the different behaviors exhibited by turbidity currents on high and low slopes.

1. Introduction

Turbidity currents are a type of gravity current in which the density difference is provided by sediment particles suspended in a fluid, often water. Hydrodynamically they are analogous to pyroclastic flows and powder snow avalanches [e.g., *Branney and Kokelaar*, 2002; *Meiburg et al.*, 2012]. Turbidity currents are volumetrically the most important mechanism for transport of sediment onto the ocean floor, often over extremely large distances and small gradients, and are responsible for the formation of submarine fans, the Earth's largest sediment accumulations. How they are able to travel so far with little frictional loss is the subject of this contribution.

Because natural turbidity currents in the ocean are infrequent, unpredictable, and commonly destroy or displace submarine monitoring equipment [*Khripounoff et al.*, 2003; *Paull et al.*, 2002], field measurements and direct constraints on their flow properties are scarce. Estimates of velocity on the relatively steep (few degrees) gradients within submarine canyons may exceed 35 ms^{-1} [*Mulder et al.*, 1997]. In the lower part of the Congo submarine canyon, where gradients are only about 0.4°, velocities up to 2.5 ms^{-1} are recorded [*Cooper et al.*, 2013].

Given the extreme scarcity of direct observation on turbidity currents, understanding of the relevant flow processes must therefore be based largely on modeling and laboratory experiments. Since the levees of submarine channels receive sediment from overbanking flows, levee heights provide some indication of the thickness of at least the largest flows [*Pirmez et al.*, 1997; *Khripounoff et al.*, 2003]. Grain sizes of sediments deposited within and at the mouths of submarine channels provide approximate estimates of the shear velocity of the currents. Gradients of the distal reaches of channels may be obtained from bathymetric data.

2. Velocity Structure

The mean velocity structure of turbidity currents as measured in the laboratory has been described by various authors [e.g., *Ellison and Turner*, 1959; *Parker et al.*, 1987; *Altinakar et al.*, 1996; *Hosseini et al.*, 2006; *Sequeiros et al.*, 2010], and the turbulence structure has been described by *Kneller et al.* [1997, 1999], *Buckee et al.* [2001], and *Baas et al.* [2005], summarized in *Kneller and Buckee* [2000] and *Meiburg and Kneller* [2010]. With few exceptions [e.g., *Sequeiros et al.*, 2010], mean velocity profiles measured in the laboratory show a velocity maximum close to the lower boundary, above a roughly logarithmic boundary layer (inner region) [e.g., *Altinakar et al.*, 1996]. The velocity distribution in the outer region of the flow (i.e., above the velocity maximum) commonly approximates to a Gaussian function [e.g., *Ellison and Turner*, 1959], though may be close to linear or exponential in supercritical currents [*Garcia*, 1990; *García*, 1993] (see also field measurements of *Xu* [2010]) and in density currents where the density difference is due to dissolved salt, which are commonly used as laboratory analogues for turbidity currents [*Ellison and Turner*, 1959; *Wilkinson and Wood*, 1972; *Parsons and*

García, 1998]. The upper part of the flow is typically dominated by Kelvin-Helmholtz instabilities associated with the shear layer between the current and the ambient sea-water [e.g., *Kneller et al*., 1999].

Field measurements of the velocity profiles have been published by *Chikita* [1989], *Normark* [1989], and *Xu* [2010], and for a cold-water density current by *Sherwin* [2010]. The velocity profile measurements of Froude supercritical currents within submarine canyons [e.g., *Xu*, 2010] approximate to an exponential profile above the velocity maximum. The form of the vertical profile of mean downstream velocity observed in both experimental and natural gravity currents is thus comparable to the velocity profile of turbulent plane wall jets [*Launder and Rodi*, 1983], and is determined largely by the balance between a logarithmic boundary layer on the lower interface and a mixing layer on the upper interface of the current [*Altinakar et al*., 1996; *Kneller et al*., 1999].

3. Density Structure

Profiles of density (i.e., concentration of suspended sediment in turbidity currents and of salt in analogous saline gravity currents) have been measured in the laboratory by *Ellison and Turner* [1959], *Wilkinson and Wood* [1972], *Parker et al*. [1987], *Garcia* [1994], *Altinakar et al*. [1996], *Choux et al*. [2005], and *Hosseini et al*. [2006]. Time-averaged values typically display a density maximum at the bed, decaying upward exponentially through the current. High-frequency fluctuations in suspended sediment distribution measured by *Baas et al*. [2005] and with higher resolution (ultrasonic high concentration meter) by *Felix et al*. [2005] clearly demonstrate coupling with the turbulence structure of the current. This kind of density profile accords fairly closely with suspended sediment distribution in shear flows in which downward settling of the grains under gravity is balanced by upward turbulent diffusion [e.g., *Middleton and Southard*, 1984; *Stacey and Bowen*, 1988]; the vertical distribution of suspended sediment is thus governed by the ratio of the settling velocity for a given particle size to the shear velocity [e.g., *Altinakar et al*., 1996; *Cantero et al*., 2009].

4. Entrainment, Drag, and Run-Out

Flows that exhibit the classic velocity profile (and K-H instabilities) are markedly nonuniform, thickening linearly downstream as a result of entrainment of ambient fluid [*Ellison and Turner*, 1959]:

$$\frac{\mathrm{d}(\bar{U}h)}{\mathrm{d}x} = E\bar{U}\,, \tag{1}$$

where E is the entrainment coefficient defined as:

$$E = \frac{E_w}{\bar{U}}\,. \tag{2}$$

In equation (2), E_w and $\bar{U}$ denote, respectively, the vertical velocity of ambient fluid into the current and the depth-averaged velocity of the current. Several studies have proposed a relationship between the entrainment coefficient, E, and bulk flow parameters, such as the bulk Richardson number, defined as:

$$Ri_0 = \frac{g'h\cos\beta}{\bar{U}^2}\,, \tag{3}$$

where β is slope, [*Ellison and Turner*, 1959; *Turner*, 1986; *Parker et al*., 1986, 1987; *Fernando*, 1991; *García*, 1993; *Wells et al*., 2010; *Johnson and Hogg*, 2013], or densimetric Froude number [e.g., *Pirmez and Imran*, 2003].

Parker et al. [1987] derived an empirical relation for E as a function of bulk Richardson number:

$$E = \frac{0.075}{\sqrt{1+718Ri_0^{2.4}}} \tag{4}$$

which predicts a gradual decrease in entrainment as Ri_0 increases, whereas that of *Turner* [1986] predicts a more abrupt shutdown of entrainment for $Ri > 0.8$ (equation (5)):

$$E = \frac{0.08-0.1Ri_0}{1+5Ri} \tag{5}$$

Both formulations (equations (4) and (5)) are based on the assumption of bulk (i.e., depth-averaged) properties.

According to several authors, the entrainment coefficient depends strongly on bottom slope [*Ellison and Turner*, 1959; *Bo Pedersen*, 1980; *Huang et al*., 2009] at least down to slopes as small as 0.5° [*Stacey and Bowen*, 1988]. Combining the analytical and numerical models of *Birman et al*. [2009] with the observations of *Nakajima and Kneller* [2013] suggests that gradients of less than about 0.6° are associated with negligible entrainment rates. Likewise *Sequeiros et al*. [2010]; *Sequeiros* [2012] observed a change from subcritical to supercritical flow at a similar value of slope. This critical value of 0.6° was also noted by *Bo Pedersen* [1980] as the slope below which the following relation could be applied:

$$E=\gamma \sin\beta \tag{6}$$

where γ takes a value of 0.072. Thus the overall drag increases with slope [*Stacey and Bowen*, 1988; *Huang et al*., 2009], and E is equivalent to an interfacial drag coefficient:

$$C_{fi}=E(1+0.5Ri_0) \tag{7}$$

[*Parker et al*., 1987]; it has been used in Chézy-type relations for the calculation of flow velocity [e.g., *Pirmez and Imran*, 2003]:

$$U^2=\frac{\sin\beta\, gCh(\rho_s-\rho_w)/\rho_w}{C_d+E} \tag{8}$$

where C is volumetric sediment concentration and C_d the coefficient of bed friction. Entrainment of ambient fluid into the current occurs predominantly via the Kelvin-Helmholtz instabilities [*Turner*, 1979, 1986], which arise where the shear due to the velocity gradient dominates over the stabilizing effect of the density gradient, this ratio being expressed by the gradient Richardson number, Ri_g:

$$Ri_g=\frac{-g\frac{\partial\rho}{\partial z}}{\rho_0\left(\frac{\partial u}{\partial z}\right)^2} \tag{9}$$

The boundary is stable when Ri_g takes a value greater than 0.25, cf. *Miles* [1961]. Note that Ri_g is equal to:

$$\frac{N^2}{\left(\frac{du}{dz}\right)^2} \tag{10}$$

with N denoting the Brunt-Väisälä (or buoyancy) frequency.

On the steep gradients of the continental slope [e.g., *Paull et al*., 2002], turbidity currents exhibit velocity profiles similar to those described above [*Xu et al*., 2004; *Xu*, 2010], and are expected to entrain ambient seawater vigorously, resulting in flow expansion. Channels on large submarine fans typically have gradients less than or much less than 0.1° and may be 0.01° or less in their distal regions [e.g., *Damuth et al*., 1995; *Khripounoff et al*., 2003], and commonly extend hundreds to thousands of kilometers from the base of the continental slope [e.g., *Babonneau et al*., 2002; *Hübscher et al*., 1997]. In order to traverse the length of these submarine fan channels such flows must be quasiconservative. Significant ambient fluid entrainment would lead to loss of channel confinement, reduced (negative) buoyancy, and consequent failure to propagate down the fan, while loss of sediment through deposition would lead to the flow's extinction. We examine the conditions that might lead to such quasiconservative behavior using numerical simulations, and subsequently compare these results with published evidence from experiments and field observations.

5. Numerical Simulations

In the following, we summarize findings from a parametric study based on a series of 2-D Navier-Stokes simulations, in order to introduce some key concepts. These qualitative observations will subsequently be put on more quantitative footing by means of fully 3-D, Large-eddy simulations (LES) for a few limited parameter combinations. All simulations were carried out for gravity-driven currents, either with a continuous inflow (Figure 1a), or in the so-called "lock-exchange configuration" (Figure 1b). The governing equations along with information on the numerical approach for their solution are provided in Appendix.

We investigate the influence of the bottom gradient on the general behavior of the gravity currents via two-dimensional simulations conducted via our in-house code TURBINS [*Nasr-Azadani and Meiburg*, 2011;

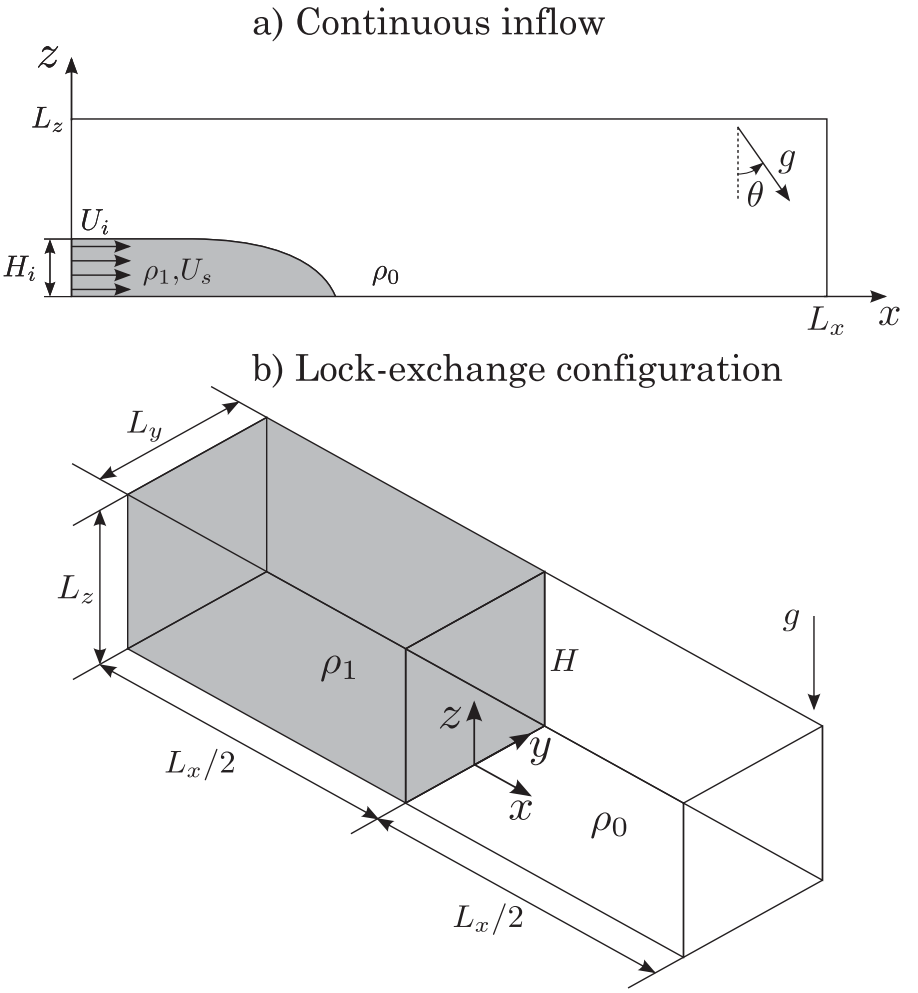

Figure 1. Schematic of (a) gravity-driven current with continuous inflow and outflow, (b) lock-exchange configuration. The grey regions represent heavy fluid of density ρ_1 penetrating into lighter ambient fluid of density ρ_0. The suspension includes particles of dimensionless settling velocity equal to U_s.

Nasr-Azadani et al., 2013]. Figure 2 compares the gravity currents with identical inlet conditions traveling on various bottom gradients; particle settling velocity was set to zero, so that these currents are analogues for turbidity currents with clay sized suspended sediment. While in all cases the conditions at the inlet are subcritical (with an inlet Froude number of 0.78), a critical bottom gradient seems to exist beyond which the K-H instabilities (and therefore the resulting entrainment and energy dissipation) grow dramatically.

Beyond this critical threshold, the velocity distribution exhibits the typical profile associated with both supercritical [e.g., *Parker et al.*, 1987] and most subcritical currents [e.g., *Kneller et al.*, 1999] based on the conventional classification of turbidity currents (see Figure 2d) via bulk densimetric Froude number. Below this threshold gradient, by contrast, the existence of stronger stratification within the shear layer at the interface between the current and the ambient fluid damps the growth of any instabilities. For the investigated cases shown in Figure 2, a gradient Richardson number less than 0.25 identifies the cases where K-H instabilities are developed in the interfacial region (see Figures 2c and 2d).

We further extend our investigation to currents with nonzero particle settling velocities, nondimensionalized using the buoyancy velocity defined as

$$u_b = \sqrt{g' \frac{H}{2}}, \tag{11}$$

where H is the channel height and g' denotes the reduced gravity. We choose the same subcritical inlet conditions and a bottom slope of 0.32° as in Figure 2. Based on a particle concentration of 0.5% and a

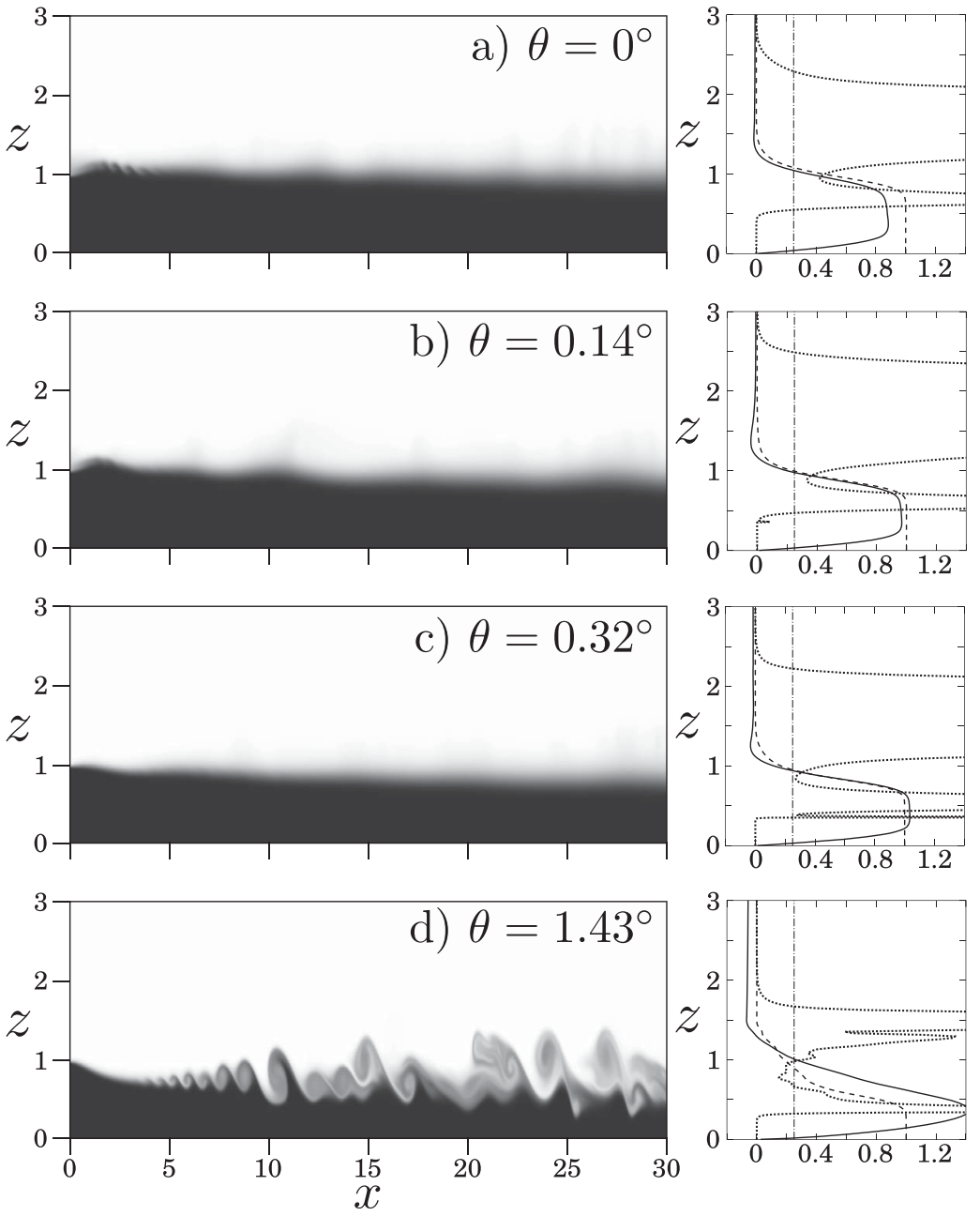

Figure 2. Influence of the bottom slope on the production of K-H instabilities and character of density-driven currents. (left) Particle concentration field shown at simulation time $t = 120$ (white and black correspond to concentration values of 0 and 1, respectively). (right) Temporal average of horizontal velocity component (solid lines), particle concentration (dashed lines), and gradient Richardson number (dots) across the current shown at stream-wise location $x = 20.5$. The vertical line indicates the Ri_g value of 0.25.

flow height of 50 m based on typical levee heights in the distal reaches of submarine fan channels [e.g., *Hübscher et al*., 1997; *Vangriesheim et al*., 2009; *Pirmez and Imran*, 2003] the dimensionless settling velocities in Figure 3 correspond to particle sizes in the medium silt to very fine sand range. Figure 3 demonstrates that smaller particles (i.e., smaller settling velocities) result in stronger density stratification along the upper interface of the current. In turn, this stronger density stratification damps the growth of any K-H instabilities (see the gradient Richardson number profiles (dots) in Figure 3), thereby reducing overall mixing, along with entrainment of ambient fluid into the turbidity current. As a result, for currents with smaller particles, the production of turbulent kinetic energy is reduced, along with dissipation, so that the resulting velocity profile becomes significantly steeper.

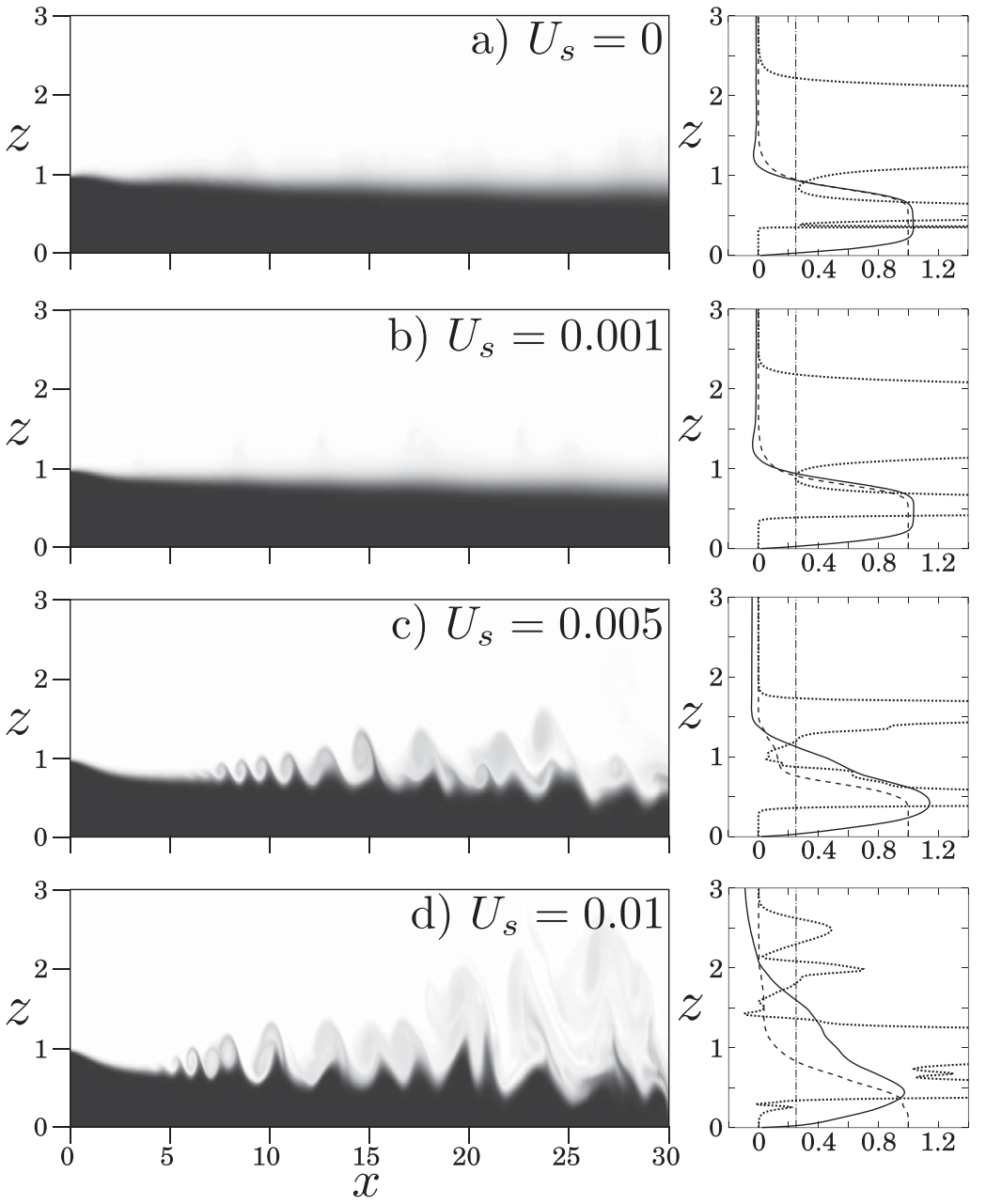

Figure 3. Influence of nondimensional particle settling velocity on the production of interfacial K-H instabilities. (left) Particle concentration field shown at simulation time $t = 120$ (white and black correspond to concentration values of 0 and 1, respectively). (right) Temporal average of horizontal velocity component (solid lines), particle concentration (dashed lines), and gradient Richardson number (dots) across the current shown at stream-wise location $x = 20.5$. The vertical line indicates the Ri_g value of 0.25.

The above concepts were verified quantitatively by means of 3-D LES simulations with a lock-exchange configuration. The LES simulations were performed at a Reynolds number of 10^5. Figure 4 demonstrates the particle concentration field for the currents with vanishing settling velocity at simulation time 30.

A direct comparison of the span-wise averaged dissipation and turbulent kinetic energy fields of currents for vanishing settling velocity (Figure 5) and (dimensionless) settling velocity equal to 0.02 (Figure 6) suggests that in the main body of the current, away from the light and dense fronts, the turbulent kinetic energy and the dissipation are greatly reduced for the current with vanishing settling velocity.

Figure 7 further demonstrates the key differences between gravity currents (vanishing settling velocity) and turbidity currents (U_s=0.02). The density gradient in the interfacial region is much higher for gravity

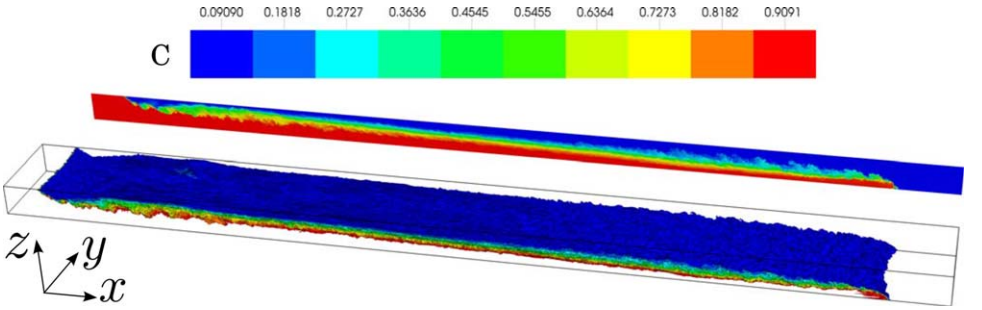

Figure 4. Contours of instantaneous concentration for a current with vanishing settling velocity ($U_s = 0$) produced by a lock-exchange configuration shown at simulation time 30.

currents as compared to turbidity currents. This results in suppressed turbulence, reflected by much reduced value for turbulent kinetic energy (TKE) and dissipation for the case of vanishing settling velocity. The decreased turbulence in the latter case is much less effective in mixing the current and the ambient, resulting in higher velocity gradient and a steeper velocity profile. Further evidence for suppression of turbulence due to stronger density gradient for the case of vanishing settling velocity can be seen in the gradient Richardson number, which exceeds 0.25 in the interfacial region.

We now estimate the necessary gradient for sustaining the turbidity current over a long distance. For a steady and sustained turbidity current, we can assume that the kinetic energy lost by the current due to dissipation must be exactly balanced by the potential energy loss as the current travels downslope. We employ the dissipation results obtained from 3-D LES simulations for currents propagating on a horizontal bottom surface in the following analysis. From the 2-D simulations, we note that the stratification is much less effective in suppressing turbulence in the interfacial region at high angles of slope. However, at low angles of

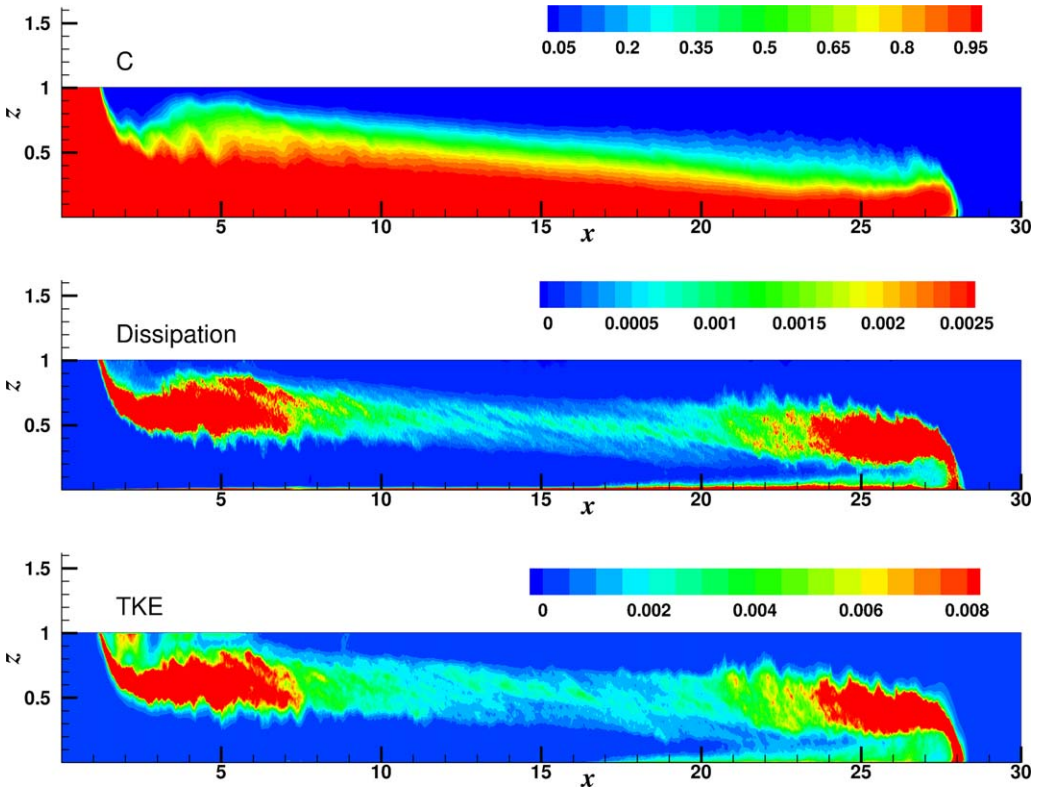

Figure 5. Contours of instantaneous span-wise averaged concentration, dissipation, and turbulent kinetic energy (TKE) for a current with vanishing settling velocity ($U_s = 0$).

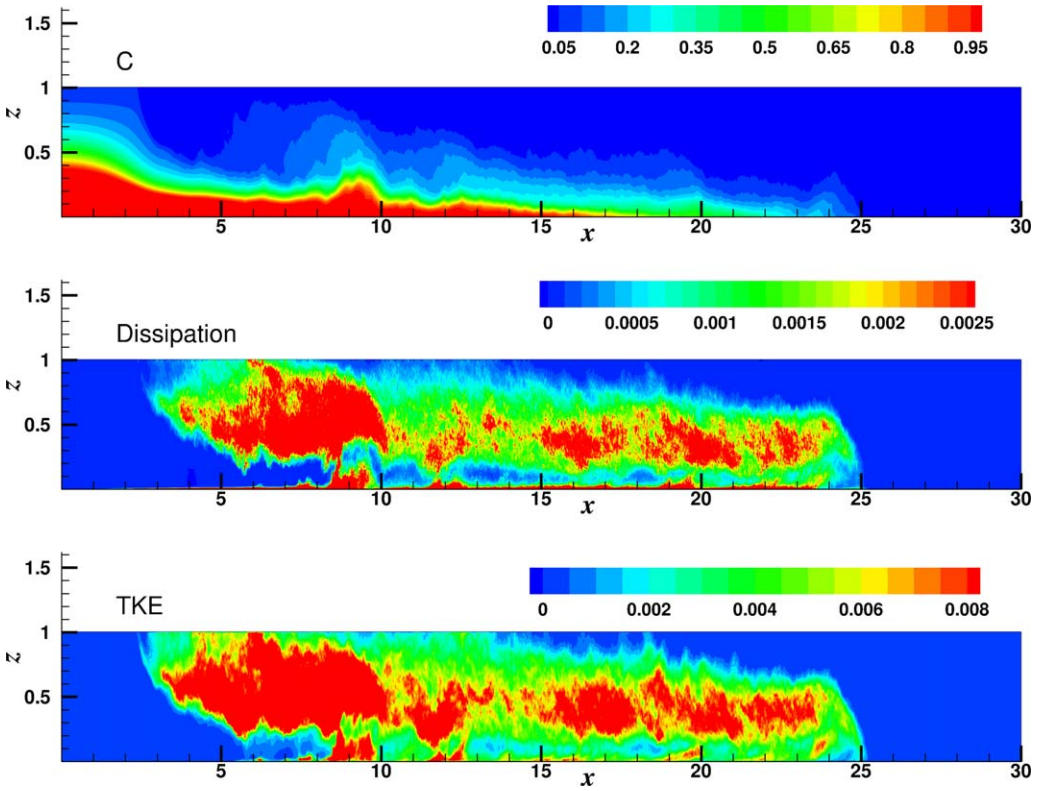

Figure 6. Contours of instantaneous span-wise averaged concentration, dissipation, and turbulent kinetic energy for a turbidity current (U_s=0.02).

slope, the stable stratification is highly effective at suppressing the turbulence in the interfacial region, and the flow evolution is similar to that observed in currents propagating on a horizontal bottom surface. Thus, the 3-D LES results obtained for currents propagating on a horizontal bottom surface should be applicable even for currents propagating over a slope, as long as the gradient is less than approximately 0.3°.

In Figure 8, consider a vertical profile of the current as it travels a distance L along the slope. Potential energy lost by the current is proportional to the vertical distance by which the center of the mass moves downward and can be calculated as:

$$\int_0^H ch \; \mathrm{d}z = c_{av} H h = c_{av} H \, L \, \sin\theta \,, \tag{12}$$

where c_{av} is the average concentration over the domain height, H. Energy loss due to dissipation over this distance L can be calculated as:

$$\int_0^H \frac{L}{u_c} \, \epsilon \; \mathrm{d}z = \epsilon_{av} H \frac{L}{u_c} \,. \tag{13}$$

Here ϵ_{av} is the average dissipation rate over H and u_c is the average current velocity. Equating energy gain to energy loss, we obtain the following expression for the angle of inclination θ

$$\sin\theta = \frac{\epsilon_{av}}{u_c c_{av}} \,. \tag{14}$$

The depth-averaged dissipation for the case of vanishing settling velocity (gravity current) from the LES simulation is 0.0004, which yields a required slope of 0.092°. For the turbidity current, the depth-averaged dissipation is 0.0016, which yields a required slope of 0.733°.

These LES simulations were performed at a Reynolds number of 10^5, at least two to three orders of magnitude lower than that for field scale flow; this difference is not expected to affect the dissipation since

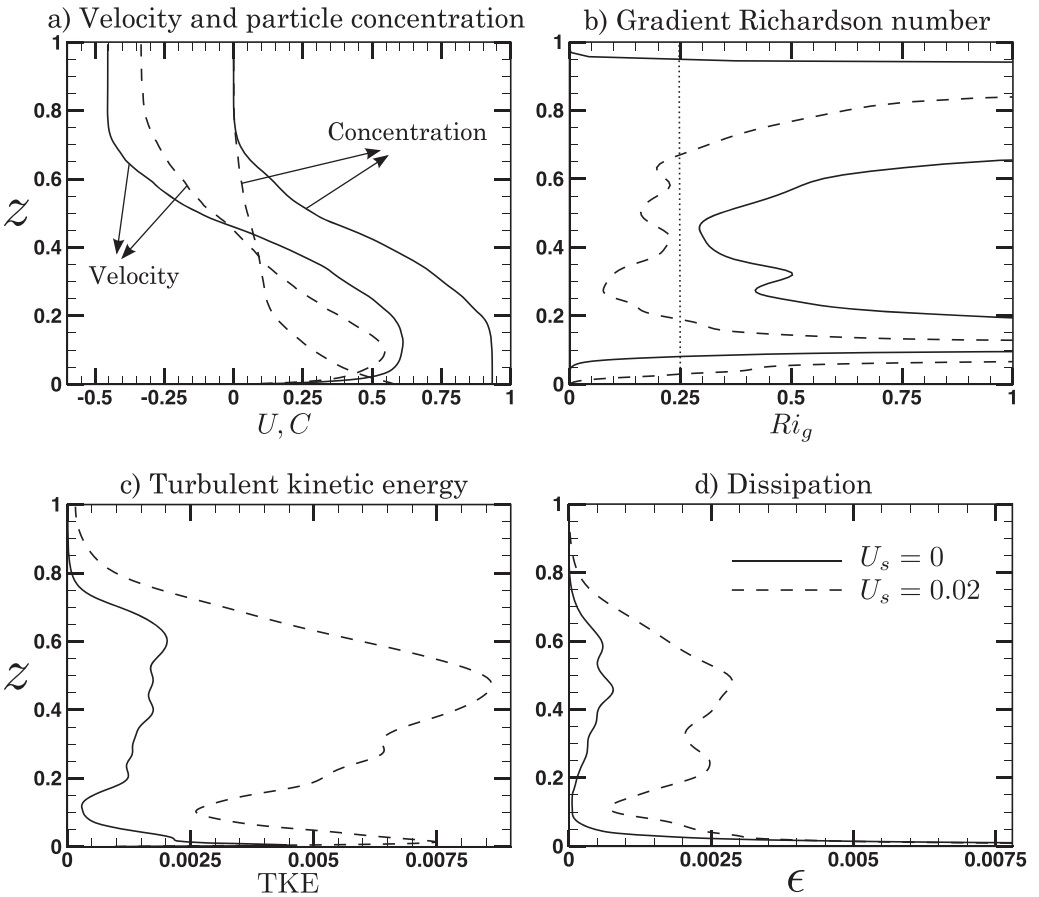

Figure 7. Comparison of vertical profiles of mean velocity, concentration, turbulent kinetic energy, dissipation, and gradient Richardson number for a current with vanishing settling velocity ($U_s = 0$, solid lines) and a turbidity current ($U_s = 0.02$, dashed lines).

dissipation in fully developed turbulence at sufficiently high Reynolds number is independent of the actual Reynolds number [cf. *Pope*, 2001].

A factor that is expected to influence the above slope estimate is the strong return flow that is present in a lock-exchange configuration. The dissipation in field scale flows, where there is no return flow, is expected to be lower than that obtained in the above analysis; thus, the slopes predicted from lock-exchange simulations are higher than would be required for sustaining a steady current in the field. Nonetheless, the slope of 0.092° obtained for the gravity current is in reasonable agreement with modal values of 0.05–0.08° for fan channels (Table 1) (after *Babonneau et al*. [2002], *Pirmez and Imran* [2003], *Vangriesheim et al*. [2009], *Cooper et al*. [2013], and data compilation in *Konsoer et al*. [2013]).

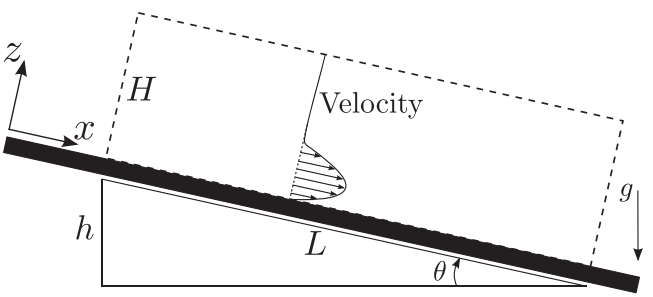

Figure 8. Schematic of the control volume utilized for energy analysis (see text for discussion).

6. Discussion

The 2-D simulations presented here appear to confirm the conclusions of several previous authors that the entrainment coefficient is a function of the bottom slope [e.g., *Ellison and Turner*, 1959; *Bo Pedersen*, 1980; *Stacey and Bowen*, 1988; *Huang et al*., 2009], which is thus a significant factor in determining the stability of the upper interface of these currents. However,

Table 1. Parameter Ranges Reported for Distal Regions of Three Large Submarine Fans

	Congo	Amazon	Bengal
Gradient of distal channel reaches	0.11° [1]	0.11° [2]	0.05° [3]
Length of channel	1100 km [4]	900 km [2]	2500 km [3]
Median sediment grain-size[b]	125–250 μm [5]	125–250 μm [2]	20–62 μm [6]
Approximate height of distal levees	70 m [1]	50 m [2]	30 m [3]
Velocity	0.7 m/s [1]	1.2 m/s [2]	

[a]Note: [1] *Vangriesheim et al*. [2009], [2] *Pirmez and Imran* [2003], [3] *Hübscher et al*. [1997], [4] *Babonneau et al*. [2002], [5] *Bonnel* [2005], and [6] *Weber et al*. [2003].
[b]31–62 μm dominant on levees; silt dominates suspended load high in flow *Vangriesheim et al*. [2009] and *Pirmez and Imran* [2003].

the bulk Richardson number (or densimetric Froude number) alone is not the main discriminant between these different behaviors [cf. *Sequeiros et al*., 2010]. *García* [1993] associated lack of entrainment with stratification effects in Froude-subcritical flow. *Cenedese et al*. [2004] and *Cenedese and Adduce* [2008] suggest that entrainment in dense currents can occur with subcritical Froude numbers, and in fact a number of experimental studies, in addition to our numerical simulations, have demonstrated that currents with densimetric Froude numbers substantially below unity may have K-H instabilities, implying $Ri_g < 0.25$ [e.g., *Hacker et al*., 1996; *Baas and Best*, 2002; *Buckee et al*., 2001; *McCaffrey et al*., 2003; *Gray et al*., 2005, 2006; *Kneller et al*., 1999]. *Cenedese and Adduce*'s [2010] parameterization of *Turner*'s [1986] entrainment relation indicates that Reynolds number is also a factor, while *Wells et al*. [2010] consider that entrainment is also a function of a flux coefficient (the ratio of the buoyancy flux to the dissipation rate). Thus while there will be a correlation between bulk Richardson number and gradient Richardson number (Ri_g) for any given set of flow conditions, there is not necessarily a simple relationship between the two. The gradient Richardson number is thus a useful measure of stability.

Both the 2-D and 3-D simulations presented in current study clearly illustrate the effect of particle settling velocity, and imply that currents in the environment dominated by very fine (clay to silt) particles are likely to have stable upper boundaries and very low entrainment coefficients. Bed roughness is also likely to have an influence (given that increased drag will result in an increase in the bulk Richardson number) but this has not been a focus of this study.

As argued above, the velocity profile of a gravity or turbidity current essentially represents the balance between a logarithmic boundary layer and a Gaussian outer layer. Where the outer layer is dominated by the instability of the shear layer at the upper boundary of the current, the velocity maximum is forced downward toward the bed, generating the classic velocity profile of most measured gravity and turbidity currents (Figures 2d, 3d, and 7a). Where the upper boundary is stable ($Ri_g > 0.25$) the logarithmic boundary layer will extend further from the wall and the velocity maximum will be displaced upward. This change in the form of the velocity profile is illustrated by both the 2-D and 3-D simulations that involve stable upper boundaries (Figures 2a–2c, 3a, 3b, and 7a). This is elegantly demonstrated by the laboratory results of *Sequeiros et al*. [2010], whose subcritical flows have velocity profiles in which the velocity maximum is displaced toward the top of the current due to the absence of K-H instabilities [$Ri_g > 0.25$], as noted by *Sequeiros et al*. [2010]. In fact the initiation of instability at the upper boundaries may occur at a densimetric Froude number deviating significantly from unity (as low as 0.4) *Kneller et al*. [1999] perhaps supporting the assertion of *Huang et al*. [2009] that the critical Froude number may be other than unity.

Another distinctive feature of these currents with stable upper boundaries is their density profile, which shows little variation in concentration below the level of the velocity maximum. This is apparent in the simulation results (Figures 2a–2c, 3a, 3b, and 7a), and in the experimental data of *Sequeiros et al*. [2010].

From the limited amount of field data available from currents in the deep ocean, there is evidence of elevated velocity maxima that may indicate the type of velocity profile observed in currents with stable upper boundaries. *Cooper et al*. [2013] reporting turbidity currents on 27 February and 10 March 2010 in the lower reaches of the Congo Canyon (with gradient 0.5°), recorded velocities at 21 m above the bed higher than those at 5 m. *Vangriesheim et al*. [2009] report velocities higher at 190 m above the bed than at 60 m in a turbidity current recorded on 24 January 2004 in the Congo Fan channel with a gradient of 0.15°.

7. Conclusions

The utility of depth-averaged parameters to describe flows whose behavior is largely determined by their density stratification is doubtful [e.g., *Huang et al*., 2009]. Our numerical results demonstrate that gradient Richardson number is a good indicator of the level of suppression of turbulence, and consequent different behaviors exhibited by turbidity currents. We conclude that turbidity currents on low gradients, especially those dominated by very fine-grained sediment (at least in their upper parts) have stable upper boundaries (with $Ri_g > 0.25$), and therefore lack Kelvin-Helmholtz instabilities. The consequences are much reduced dissipation and a vanishingly small entrainment coefficient, both of which contribute to these flows' ability to traverse immense distances over the ocean floor.

Appendix A: Numerical Method

A1. Two-Dimensional Simulations

Our in-house code TURBINS is a finite-difference code that solves the incompressible Navier-Stokes equation in Boussinesq approximations. TURBINS employs a fractional projection method along with the third-order TVD-RK3 time integration. Spatial discretization is implemented via second-order finite difference for the diffusive terms and third-order ENO scheme for the convective terms (for numerical details and validations, see *Nasr-Azadani and Meiburg* [2011] and *Nasr-Azadani et al*. [2013]).

The computational details of all the two-dimensional simulations are as follows. The computational domain size is $L_x \times L_z = 60 \times 5$. At the inlet, we define a uniform flux of suspension into the control volume. The resulting Froude number is defined as the ratio of inlet velocity to the buoyancy velocity. Reynolds number, defined via the buoyancy velocity, inlet height, and kinematic viscosity of water, is set to 5000. Flow velocity is rendered dimensionless using the buoyancy velocity.

To evolve the particle field, we employ an Eulerian approach with a continuous concentration field $c(x, y, z)$. It is then evolved via an advection-diffusion transport equation (see *Necker et al*. [2002] for details). The resulting Schmidt number is set to unity. A nonuniform grid is generated in the z-direction. In the vicinity of the bottom wall, grid is chosen with spacing equal to 0.0033 and stretched smoothly to 0.04 at the top wall. We employ a uniform grid with spacing 0.02 in the x-direction.

A2. Three-Dimensional Simulations

The three-dimensional simulations presented above were conducted using Large-eddy simulation (LES) as a turbulence model. In LES, only the energy-containing large "eddie" are resolved, while all the scales of motion below a cutoff (this includes the dissipative scales) are modeled. This cutoff is determined by a filter width, which is often dependent on the grid spacing used in the simulation. The effect of all the scales of the motion below this filter width appear as additional subgrid-scale stress (SGS stress) terms in the governing Navier-Stokes for momentum, and as a subgrid flux (SGS flux) term in the concentration transport equation.

The governing equations are obtained by filtering the nondimensional Navier-Stokes and the concentration transport equations. The filtered equations are of the form

$$\frac{\partial \bar{u}_i}{\partial t} + \frac{\partial \left(\bar{u}_i \overline{u_j}\right)}{\partial x_j} = -\frac{\partial \bar{p}}{\partial x_i} + \frac{1}{Re}\frac{\partial^2 \bar{u}_i}{\partial x_j \partial x_j} - \frac{\partial \tau_{ij}}{\partial x_j} - \bar{c}\delta_{i3}\,, \tag{15}$$

$$\frac{\partial \bar{c}}{\partial t} + \frac{\partial \left(\bar{c}\,\overline{u_j}\right)}{\partial x_j} = \frac{1}{Sc \cdot Re}\frac{\partial^2 \bar{c}}{\partial x_j \partial x_j} - \frac{\partial \eta_j}{\partial x_j}\,. \tag{16}$$

Here we set the molecular Schmidt number (Sc) to unity. In our LES approach, the SGS terms (τ_{ij} and η_j) are modeled using the Smagorinsky model. The SGS stresses are thus calculated using

$$\tau_{ij} - \frac{1}{3}\tau_{kk}\delta_{ij} = -2\nu_t \bar{S}_{ij}\,, \tag{17}$$

where ν_t is the SGS eddy viscosity, which is calculated using

$$\nu_t = (C_s \Delta)^2 |\bar{S}|\,. \tag{18}$$

Here $\bar{S}_{ij}$ is the strain rate tensor, Δ is a length scale proportional to the local grid spacing, and C_s is the model coefficient. The SGS flux terms are calculated using

$$\eta_j = -\frac{\nu_t}{Sc_t}\frac{\partial \bar{c}}{\partial x_j}. \quad (19)$$

The governing equations are solved using a second-order finite-difference LES code that uses energy-conservative discretization. The LES code uses second-order central difference scheme for discretizing both the convective and the diffusive terms. All terms except the wall-normal diffusive terms are advanced explicitly in time using a third-order Runge-Kutta method. The wall-normal diffusive terms are advanced implicitly using a second-order Crank-Nicolson method. The model coefficient C_s and the SGS Schmidt number Sc_t are computed using a dynamic model [*Germano et al*., 1991; *Moin et al*., 1991].

The LES simulations were performed on a computational domain of size, $L_x \times L_y \times L_z = 30 \times 3 \times 1$. The simulations used a computational grid with $N_x \times N_y \times N_z = 3,000 \times 450 \times 200$ nodes. The Reynolds number based on the buoyancy velocity and the height of the domain is 10^5. Particle settling velocity is nondimensionalized by the buoyancy velocity and is set to $U_s = 0.02$.

Acknowledgments
We thank Octavio Sequeiros and an anonymous reviewer for constructive and helpful reviews. We acknowledge the funding provided by sponsors BG Group, BP, DONG, PetroChina, RWE Dea, Statoil, and Tullow Oil under joint industry project PRACSS. The source code TURBINS is freely available from authors upon request. The data and input files required to reproduce the simulations with TURBINS as well as simulation results are available from the authors upon request (meiburg@engineering.ucsb.edu), and are archived at the Computational Fluid Dynamics Laboratory (CFD-Lab), Mechanical Engineering Department at the University of California at Santa Barbara.

References

Altinakar, M. S., W. H. Graf, and E. J. Hopfinger (1996), Flow structure in turbidity currents, *J. Hydraul. Res.*, *34*(5), 713–718.
Baas, J. H., and J. L. Best (2002), Turbulence modulation in clay-rich sediment-laden flows and some implications for sediment deposition, *J. Sediment. Res.*, *72*(3), 336–340.
Baas, J. H., W. D. McCaffrey, P. D. W. Haughton, and C. Choux (2005), Coupling between suspended sediment distribution and turbulence structure in a laboratory turbidity current, *J. Geophys. Res.*, *110*, C11015, doi:10.1029/2004JC002668.
Babonneau, N., B. Savoye, M. Cremer, and B. Klein (2002), Morphology and architecture of the present canyon and channel system of the Zaire deep-sea fan, *Mar. Pet. Geol.*, *19*(4), 445–467.
Birman, V. K., E. Meiburg, and B. Kneller (2009), The shape of submarine levees: Exponential or power law?, *J. Fluid Mech.*, *619*, 367–376.
Bonnel, C. (2005), Mise en place des lobes distaux dans les systèmes turbiditiques actuels: analyse comparée des sysytèmes du Zaïre, Var, et Rhône, PhD thesis, L'Universite Bordeaux I., Bordeaux, France.
Bo Pedersen, F. (1980), A monograph on turbulent entrainment and friction in 2-layer stratified flow, *Ser. Pap. 25*, 397 pp., Inst. of Hydrodyn. and Hydraul. Eng., Technical University of Denmark, Lungby.
Branney, M. J., and B. P. Kokelaar (2002), *Pyroclastic Density Currents and the Sedimentation of Ignimbrites*, Geol. Soc. of London, London.
Buckee, C., B. Kneller, and J. Peakall (2001), Turbulence structure in steady, solute-driven gravity currents, in *Particulate Gravity Currents, Spec. Publ., 31*, edited by W. McCaffrey, B. C. Kneller, and J. Peakall, pp. 173–188, Int. Assoc. Sedimentol., Wiley, New York.
Cantero, M. I., S. Balachandar, A. Cantelli, C. Pirmez, and G. Parker (2009), Turbidity current with a roof: Direct numerical simulation of self-stratified turbulent channel flow driven by suspended sediment, *J. Geophys. Res.*, *114*, C03008, doi:10.1029/2008JC004978.
Cenedese, C., and C. Adduce (2008), Mixing in a density-driven current flowing down a slope in a rotating fluid, *J. Fluid Mech.*, *604*, 369–388.
Cenedese, C., and C. Adduce (2010), A new parameterization for entrainment in overflows, *J. Phys. Oceanogr.*, *40*(8), 1835–1850.
Cenedese, C., J. A. Whitehead, T. A. Ascarelli, and M. Ohiwa (2004), A dense current flowing down a sloping bottom in a rotating fluid, *J. Phys. Oceanogr.*, *34*(1), 188–203.
Chikita, K. (1989), A field study on turbidity currents initiated from spring runoffs, *Water Resour. Res.*, *25*(2), 257–271.
Choux, C. M. A., J. H. Baas, W. D. McCaffrey, and P. D. W. Haughton (2005), Comparison of spatio-temporal evolution of experimental particulate gravity flows at two different initial concentrations, based on velocity, grain size and density data, *Sediment. Geol.*, *179*(1), 49–69.
Cooper, C., J. Wood, and O. Andrieux (2013), Turbidity current measurements in the Congo Canyon, in *Proceedings of the Annual Offshore Technology Conference (OTC 23992)*, Offshore Technology Conference, Houston, Tex.
Damuth, J. E., R. D. Flood, C. Pirmez, and P. L. Manley (1995), Architectural elements and depositional processes of amazon deep-sea fan imaged by long-range sidescan sonar (gloria), bathymetric swath-mapping (sea beam), high-resolution seismic and piston-core data, in *Atlas of Deep Water Environments*, edited by K. T. Pickering et al., pp. 105–121, Springer, Dordrecht, Netherlands.
Ellison, T. H., and J. S. Turner (1959), Turbulent entrainment in stratified flows, *J. Fluid Mech.*, *6*(3), 423–448.
Felix, M., S. Sturton, and J. Peakall (2005), Combined measurements of velocity and concentration in experimental turbidity currents, *Sediment. Geol.*, *179*(1), 31–47.
Fernando, H. J. S. (1991), Turbulent mixing in stratified fluids, *Annu. Rev. Fluid Mech.*, *23*(1), 455–493.
Garcia, M. H. (1990), Depositing and eroding sediment-driven flows: Turbidity currents, *Project Rep. 306*, St. Anthony Falls Hydraul. Lab, University of Minnesota, Minn.
García, M. H. (1993), Hydraulic jumps in sediment-driven bottom currents, *J. Hydraul. Eng.*, *119*(10), 1094–1117.
Garcia, M. H. (1994), Depositional turbidity currents laden with poorly sorted sediment, *J. Hydraul. Eng.*, *120*(11), 1240–1263.
Germano, M., U. Piomelli, P. Moin, and W. H. Cabot (1991), A dynamic subgrid-scale eddy viscosity model, *Phys. Fluids A*, *3*(7), 1760–1765.
Gray, T. E., J. Alexander, and M. R. Leeder (2005), Quantifying velocity and turbulence structure in depositing sustained turbidity currents across breaks in slope, *Sedimentology*, *52*(3), 467–488.
Gray, T. E., J. Alexander, and M. R. Leeder (2006), Longitudinal flow evolution and turbulence structure of dynamically similar, sustained, saline density and turbidity currents, *J. Geophys. Res.*, *111*, C08015, doi:10.1029/2005JC003089.
Hacker, J., P. F. Linden, and S. B. Dalziel (1996), Mixing in lock-release gravity currents, *Dyn. Atmos. Oceans*, *24*(1), 183–195.
Hosseini, S. A., A. Shamsai, and B. Ataie-Ashtiani (2006), Synchronous measurements of the velocity and concentration in low density turbidity currents using an acoustic Doppler velocimeter, *Flow Meas. Instrum.*, *17*(1), 59–68.
Huang, H., J. Imran, C. Pirmez, Q. Zhang, and G. Chen (2009), The critical densimetric Froude number of subaqueous gravity currents can be non-unity or non-existent, *J. Sediment. Res.*, *79*(7), 479–485.

Hübscher, C., V. Spieβ, M. Breitzke, and M. E. Weber (1997), The youngest channel-levee system of the Bengal Fan: Results from digital sediment echosounder data, *Mar. Geol.*, *141*(1), 125–145.
Johnson, C. G., and A. J. Hogg (2013), Entraining gravity currents, *J. Fluid Mech.*, *731*, 477–508.
Khripounoff, A., A. Vangriesheim, N. Babonneau, P. Crassous, B. Dennielou, and B. Savoye (2003), Direct observation of intense turbidity current activity in the Zaire submarine valley at 4000 m water depth, *Mar. Geol.*, *194*(3), 151–158.
Kneller, B., and C. Buckee (2000), The structure and fluid mechanics of turbidity currents: A review of some recent studies and their geological implications, *Sedimentology*, *47*(s1), 62–94.
Kneller, B. C., S. J. Bennett, and W. D. McCaffrey (1997), Velocity and turbulence structure of density currents and internal solitary waves: Potential sediment transport and the formation of wave ripples in deep water, *Sediment. Geol.*, *112*(3), 235–250.
Kneller, B. C., S. J. Bennett, and W. D. McCaffrey (1999), Velocity structure, turbulence and fluid stresses in experimental gravity currents, *J. Geophys. Res.*, *104*(C3), 5381–5391.
Konsoer, K., J. Zinger, and G. Parker (2013), Bankfull hydraulic geometry of submarine channels created by turbidity currents: Relations between bankfull channel characteristics and formative flow discharge, *J. Geophys. Res. Earth Surf.*, *118*, 216–228, doi:10.1029/2012JF002422.
Launder, B. E., and W. Rodi (1983), The turbulent wall jet measurements and modeling, *Annu. Rev. Fluid Mech.*, *15*(1), 429–459.
McCaffrey, W. D., C. M. Choux, J. H. Baas, and P. D. W. Haughton (2003), Spatio-temporal evolution of velocity structure, concentration and grain-size stratification within experimental particulate gravity currents, *Mar. Pet. Geol.*, *20*(6), 851–860.
Meiburg, E., and B. Kneller (2010), Turbidity currents and their deposits, *Annu. Rev. Fluid Mech.*, *42*(1), 135–156.
Meiburg, E., J. McElwaine, B. Kneller, and H. Fernando (2012), Turbidity currents and powder snow avalanches, in *Environmental Fluid Dynamics Handbook*, edited by H. J. S. Fernando, pp. 557–573, CRC Press, Boca Raton, Fla.
Middleton, G. V., and J. B. Southard (1984), *Mechanics of sediment movement, Short Course Lecture Notes 3*, Soc. Econ. Pal. Mineral, Tulsa, Okla.
Miles, J. W. (1961), On the stability of heterogeneous shear flows, *J. Fluid Mech.*, *10*(4), 496–508.
Moin, P., K. Squires, W. Cabot, and S. Lee (1991), A dynamic subgrid-scale model for compressible turbulence and scalar transport, *Phys. Fluids A*, *3*(11), 2746–2757.
Mulder, T., B. Savoye, and J. P. M. Syvitski (1997), Numerical modelling of a mid-sized gravity flow: The 1979 nice turbidity current (dynamics, processes, sediment budget and seafloor impact), *Sedimentology*, *44*(2), 305–326.
Nakajima, T., and B. C. Kneller (2013), Quantitative analysis of the geometry of submarine external levees, *Sedimentology*, *60*(4), 877–910.
Nasr-Azadani, M. M., and E. Meiburg (2011), TURBINS: An immersed boundary, Navier-Stokes code for the simulation of gravity and turbidity currents interacting with complex topographies, *Comput. Fluids*, *45*(1), 14–28.
Nasr-Azadani, M. M., B. Hall, and E. Meiburg (2013), Polydisperse turbidity currents propagating over complex topography: Comparison of experimental and depth-resolved simulation results, *Comput. Geosci.*, *53*, 141–153.
Necker, F., C. Härtel, L. Kleiser, and E. Meiburg (2002), High-resolution simulations of particle-driven gravity currents, *Int. J. Multiphase Flow*, *28*(2), 279–300.
Normark, W. R. (1989), Observed parameters for turbidity-current flow in channels, reserve fan, lake superior, *J. Sediment. Res.*, *59*(3), 423–431.
Parker, G., Y. Fukushima, and H. M. Pantin (1986), Self-accelerating turbidity currents, *J. Fluid Mech.*, *171*, 145–181.
Parker, G., M. Garcia, Y. Fukushima, and W. Yu (1987), Experiments on turbidity currents over an erodible bed, *J. Hydraul. Res.*, *25*(1), 123–147.
Parsons, J. D., and M. H. García (1998), Similarity of gravity current fronts, *Phys. Fluids*, *10*(12), 3209–3213.
Paull, C. K., W. Ussler III, H. G. Greene, R. Keaten, P. Mitts, and J. Barry (2002), Caught in the act: The 20 December 2001 gravity flow event in Monterey Canyon, *Geo Mar. Lett.*, *22*(4), 227–232.
Pirmez, C., and J. Imran (2003), Reconstruction of turbidity currents in Amazon Channel, *Mar. Pet. Geol.*, *20*(6), 823–849.
Pirmez, C., R. N. Hiscott, and J. D. Kronen (1997), Sandy turbidite successions at the base of channel-levee systems of the amazon fan revealed by FMS logs and cores: Unraveling the facies architecture of large submarine fans, *Proc. Ocean Drill. Program Sci. Res.*, *155*, 7–33.
Pope, S. B. (2001), Turbulent flows, *Meas. Sci. Technol.*, *12*(11), 2020.
Sequeiros, O. E. (2012), Estimating turbidity current conditions from channel morphology: A Froude number approach, *J. Geophys. Res.*, *117*, C04003, doi:10.1029/2011JC007201.
Sequeiros, O. E., B. Spinewine, R. T. Beaubouef, T. Sun, M. H. García, and G. Parker (2010), Characteristics of velocity and excess density profiles of saline underflows and turbidity currents flowing over a mobile bed, *J. Hydraul. Eng.*, *136*(7), 412–433.
Sherwin, T. J. (2010), Observations of the velocity profile of a fast and deep oceanic density current constrained in a gully, *J. Geophys. Res.*, *115*, C03013, doi:10.1029/2009JC005557.
Stacey, M. W., and A. J. Bowen (1988), The vertical structure of turbidity currents and a necessary condition for self-maintenance, *J. Geophys. Res.*, *93*(C4), 3543–3553.
Turner, J. S. (1979), *Buoyancy Effects in Fluids*, Cambridge Univ. Press, Cambridge, U. K.
Turner, J. S. (1986), Turbulent entrainment: The development of the entrainment assumption, and its application to geophysical flows, *J. Fluid Mech.*, *173*, 431–471.
Vangriesheim, A., A. Khripounoff, and P. Crassous (2009), Turbidity events observed in situ along the Congo submarine channel, *Deep Sea Res., Part II*, *56*(23), 2208–2222.
Weber, M. E., M. Wiedicke-Hombach, H. R. Kudrass, and H. Erlenkeuser (2003), Bengal Fan sediment transport activity and response to climate forcing inferred from sediment physical properties, *Sediment. Geol.*, *155*(3), 361–381.
Wells, M., C. Cenedese, and C. P. Caulfield (2010), The relationship between flux coefficient and entrainment ratio in density currents, *J. Phys. Oceanogr.*, *40*(12), 2713–2727.
Wilkinson, D. L., and I. R. Wood (1972), Some observations on the motion of the head of a density current, *J. Hydraul. Res.*, *10*(3), 305–324.
Xu, J. P. (2010), Normalized velocity profiles of field-measured turbidity currents, *Geology*, *38*(6), 563–566.
Xu, J. P., M. A. Noble, and L. K. Rosenfeld (2004), In-situ measurements of velocity structure within turbidity currents, *Geophys. Res. Lett.*, *31*, L09311, doi:10.1029/2004GL019718.